Commun. Comput. Phys.
doi: 10.4208/cicp.010909.010410a

Vol. **9**, No. 1, pp. 147-179
January 2011

An Optimized Perfectly Matched Layer for the Schrödinger Equation

Anna Nissen* and Gunilla Kreiss

Department of Information Technology, Uppsala University, P.O. Box 337, SE-75105 Uppsala, Sweden.

Received 1 September 2009; Accepted (in revised version) 1 April 2010

Available online 5 August 2010

Abstract. We derive a perfectly matched layer (PML) for the Schrödinger equation using a modal ansatz. We derive approximate error formulas for the modeling error from the outer boundary of the PML and the error from the discretization in the layer and show how to choose layer parameters so that these errors are matched and optimal performance of the PML is obtained. Numerical computations in 1D and 2D demonstrate that the optimized PML works efficiently at a prescribed accuracy for the zero potential case, with a layer of width less than a third of the de Broglie wavelength corresponding to the dominating frequency.

AMS subject classifications: 35B65, 35P25, 35Q41, 65M06, 65M15

Key words: Schrödinger equation, perfectly matched layer.

1 Introduction

Propagating waves are important in many fields of applications, such as electromagnetism, acoustics, aerodynamics and quantum mechanics. These types of problems are often formulated on very large or unbounded domains and an important aspect in performing efficient numerical simulations is to restrict the original domain to a much smaller computational domain. In order to mimic the behavior of outgoing waves on an unbounded domain, artificial boundary conditions need to be imposed on the boundary of the computational domain. An important feature of this boundary is that it should not reflect outgoing waves, which would contaminate the solution of the original problem. Such artificial boundary conditions can be divided into two classes: non-reflecting or absorbing boundary conditions (ABC) and absorbing layers. An ABC is posed precisely on the boundary, whereas an absorbing layer is an extension of the computational

*Corresponding author. *Email addresses:* anna.nissen@it.uu.se (A. Nissen), gunilla.kreiss@it.uu.se (G. Kreiss)

domain where outgoing waves are dampened (see, e.g., Hagstrom [1, 2] and Givoli [3] for extensive reviews on ABCs).

Here, we consider solving the time-dependent Schrödinger equation with a member from the second class, a perfectly matched layer (PML), in order to study the behavior of quantum mechanical systems without having spurious reflections from waves traveling out of the domain. This is an important issue when studying the dynamics of a chemical reaction, e.g., when the quantum mechanical system consists of a molecule that dissociates into two smaller molecules with a certain probability. The Schrödinger equation is formulated in terms of a wavefunction, where the squares of the absolute values of the wavefunction give the probability density of the states of the system. For the dissociating molecule, this means that as the distance between the two subsystems increases a "probability cloud" propagates towards the far-field. Another application of interest is quantum optimal control. Through the calculation of pulse shapes, e.g., finding the optimal shape of a laser pulse that drives a system from one state to another in a finite time, the control of chemical reactions is enabled. If the problem at hand can experience dissociation, absorbing boundary conditions should be imposed to take care of boundary effects [4].

The perfectly matched layer (PML) method was developed for Maxwell's equations by Berenger [5] in 1994 and has been successfully used in computational electromagnetics, where it has become the standard method. The idea of the PML method is to surround the computational domain by an artificial damping layer of finite width, where a modified set of equations have to be solved. Ideally, the incoming waves are damped to such an extent that the outer boundary conditions are of no importance. Also, the interface between the computational domain and the damping layer should not cause any reflections. The PML fulfils this criteria in theory, although some reflections occur in practice due to the discretization of the problem. We will refer to these as numerical reflections.

In comparison, much work has been done on developing exact ABCs and local approximations of ABCs for the Schrödinger equations. See for instance the review article of Antoine et al. [6]. A very recent result is Jiang and Greengard [7], where a fast algorithm for the exact, global condition is presented. However, specific geometries are required for global ABCs and extension to multi-dimensions is not trivial. Alternatively, local conditions can be derived for a more efficient implementation, at the expense of accuracy. The PML method is not as restricted as ABCs in terms of geometries and application in several dimensions, which makes it suitable for large-scale problems. Also, the PML approach is closely related to absorbing boundary methods used in chemical physics, and our results can be extended to such methods.

The aim of this work is to show how to systematically choose damping parameters and discretization parameters for optimal performance of a Schrodinger PML. A related study for Maxwell's equations in second order formulation was done in [8]. We focus on spatial discretization by finite difference methods and consider orders 2, 4, 6 and 8. In time we use a finite difference scheme of order 2, but the study is also relevant for more efficient time propagation methods. In particular we have the Magnus-Arnoldi

schemes [9] in mind.

The disposition of the article is as follows: in Section 1.1, we give an overview of the relevant absorbing layers in chemical physics. In Section 2, the modified PML equation is derived and the relation between smooth exterior scaling (SES) and PML is discussed. Finally, well-posedness is discussed. We consider numerical approximations in Section 3. Error analysis is considered in Section 4, where we derive approximate formulas for numerical errors and the error caused by the finite width of the layer. Numerical experiments in 1D and 2D are performed in Sections 5 and 6, respectively, verifying the error formulas derived in Section 4 and demonstrating how these yield optimal results. Conclusions are given in Section 7.

1.1 Damping layers in quantum dynamics

An important task in the field of chemical physics is to calculate the energies of resonance states. A resonance state is defined as a long-lived state of a system, which has sufficient energy to break up into two or more subsystems [10]. In scattering experiments, the subsystems can for instance be an electron, which is scattered from an atom or a molecule. The resonance states have a coupling to the continuous spectra of the Hamiltonian and are associated with eigenfunctions, which are not square integrable. In order to enable the use of basis expansion methods, the problem needs to reformulated so that the corresponding eigenfunctions are normalizable. There are different techniques that address this issue, the common denominator being that the Hamiltonian of the reformulated system is no longer Hermitian. One technique is complex scaling, where a coordinate transformation

$$x \to F(x) = xe^{i\theta},$$

into the complex plane leads to square integrability of the resonance wave eigenfunctions, while the resonance energies remain unaffected [10]. Using complex scaling for molecular problems means that a potential energy surface (PES), which is given as a set of *ab initio* points, needs to be scaled and interpolated between the points by analytic functions. Smooth exterior scaling (SES) is based on the theory of complex scaling, but the coordinate transformation occurs after some $x = x_1$, after which the PES is assumed to be constant. Hence, by using the SES technique the scaling of the PES can be avoided. However, the most common approach in chemical physics is to add a complex absorbing potential (CAP) to the physical Hamiltonian right outside the domain of interest. The main reason that the CAPs are so popular is that they are easy to implement together with pseudospectral methods, a diagonal complex matrix is simply added to the discretized Hamiltonian. However, the spectrum of the perturbed Hamiltonian will be affected when applying the CAP method for energy calculations. In dynamic settings this effect corresponds to unphysical reflections. A significant advantage for SES and complex scaling over CAP is that they stand on a more rigorous mathematical ground [11].

2 The Schrödinger equation

We consider the time-dependent Schrödinger equation in two space dimensions

$$i\frac{\partial u}{\partial t} = -\frac{\partial^2 u}{\partial x^2} + L\Big(y, \frac{\partial}{\partial y}\Big)u, \qquad \text{in } \Omega = [x_0, \infty) \times [-l, l], \quad t \geq 0, \tag{2.1}$$

with homogeneous boundary conditions at $y = \pm l$. We assume that L in concert with these boundary conditions is a Sturm-Liouville problem, where

$$L\Big(y, \frac{\partial}{\partial y}\Big) = -\frac{\partial^2}{\partial y^2} + V(y), \tag{2.2}$$

with eigenvalues κ_j^2 and eigenvectors ψ_j

$$L\psi_j = \kappa_j^2 \psi_j, \qquad j = 1, \cdots, \infty.$$

$V(y)$ is called the potential.

Further, we consider a Dirichlet condition at $x = x_0$

$$u(x_0, y, t) = 0, \qquad -l \leq y \leq l, \ \ t \geq 0,$$

and a decay condition

$$\lim_{x \to \infty} u(x, y, t) = 0, \qquad -l \leq y \leq l, \ \ t \geq 0. \tag{2.3}$$

We assume compactly supported initial data $u_0(x, y)$ in the domain of interest

$$\Omega_I = [x_0, x_1] \times [-l, l],$$

so that u is initially zero in

$$\Omega_O = [x_1, \infty) \times [-l, l].$$

2.1 Bound states and dissociative states

The assumption of a Sturm-Liouville operator (2.2) corresponds to the existence of a potential barrier, i.e., solutions with localized wavefunctions are supported. In an eigenvalue setting, these are corresponding solutions called bound states, i.e., localized eigenfunctions with corresponding discrete eigenvalues. Bound states appear when at least two particles are joined, and cannot be separated unless sufficient energy is added to the system. If sufficient energy is added to the system, the particles may dissociate. This corresponds to parts of the probability density function escaping the potential barrier and leaving the computational domain. For such cases there is a need for absorbing boundary conditions at the edge of the computational domain. Dissociation corresponds to the

existence of so-called dissociative states, which are non-local eigenfunctions with eigenvalues in the continuous spectra.

In (2.1), we assume the potential to be independent of x, i.e., we consider the Schrödinger equation for a free particle in the x-direction. However, without restriction, an x-dependent potential can be considered if it is independent of x, for $x \geq x_1$. Under these conditions, both bound states and dissociative states can appear. The solutions with low energies will be trapped in the potential and only solutions with sufficiently high energy escape the potential barrier and leave the computational domain. In this paper, we are interested in the dissociative process, which under our assumptions only is possible in the x-direction.

2.2 The Schrödinger equation with PML

We want to truncate the infinite domain in the x-direction by constructing a PML of width d beginning at $x=x_1$, so that the new domain, constituted by the interior domain, Ω_I, and the adjacent PML, is reduced to

$$\Omega_C = [x_0, x_1+d] \times [-l,l].$$

We denote Ω_C the computational domain. There are other choices than the Dirichlet condition at $x = x_0$, for instance a PML could be constructed also there. However, we consider only the right side of the spatial domain, since it is unlikely that we would need layers both in the positive and negative x-directions for our application.

The Schrödinger equation in the PML is modified following Hagstrom [2]. We consider the domain outside the interior domain

$$\Omega_O = [x_1, \infty) \times [-l,l].$$

Expanding u in the ψ_j's and Laplace-transforming in time gives the equation

$$is\hat{u}_j = -\frac{\partial^2 \hat{u}_j}{\partial x^2} + \kappa_j^2 \hat{u}_j, \tag{2.4}$$

with solutions

$$\hat{u}_j(x) = A_j e^{\lambda_+ (x-x_1)} + B_j e^{\lambda_- (x-x_1)}, \tag{2.5}$$

where

$$\lambda_\pm = \pm\sqrt{-is+\kappa_j^2}.$$

We want to modify (2.5), so that waves that propagate into the layer are damped. We consider $Re(s) \geq 0$ and choose the branch of the square root, so that

$$Re\left(\sqrt{-is+\kappa_j^2}\right) \geq 0, \qquad \text{for } \; Re(s) \geq 0.$$

In physical space, the component in (2.5) with coefficient A_j corresponds to a left-going wave and the component with coefficient B_j to a right-going wave. Due to the choice of the square root λ_- gives bounded solutions that satisfy (2.3) and decaying waves can be obtained by modifying the exponent in the following way

$$\hat{u}_{j,PML}(x) = B_j \exp\Big[-\sqrt{-is+\kappa_j^2}\Big((x-x_1)+e^{i\gamma}\int_{x_1}^{x}\sigma(\omega)\mathrm{d}\omega\Big)\Big], \tag{2.6}$$

where $\sigma(\omega)$ is a real, non-negative function in ω, called the absorption function. Polynomial absorption functions are used throughout the paper. The parameter γ is usually a constant grid stretching parameter chosen as $0<\gamma<\pi/2$, in order to obtain decaying solutions. An alternative is to let γ vary with x in the PML, i.e., $\gamma=\gamma(x)$. For perfect matching the solution and its derivative in the interior domain should coincide with the modified solution and its derivative in the layer at the interface $x=x_1$. Thus we need to impose the additional condition

$$\sigma(x_1)=0.$$

The modified expression (2.6) satisfies

$$i\frac{\partial u}{\partial t} = -\frac{1}{1+e^{i\gamma}\sigma(x)}\frac{\partial}{\partial x}\frac{1}{1+e^{i\gamma}\sigma(x)}\frac{\partial u}{\partial x}+L\Big(y,\frac{\partial}{\partial y}\Big)u, \tag{2.7}$$

in

$$\Omega_C=[x_0,x_1+d]\times[-l,l],$$

instead of (2.1). Note that if

$$\sigma(x)=0, \quad \text{for } x\le x_1,$$

(2.7) reduces to (2.1) in the interior domain, Ω_I. Hence, we can solve (2.7) both in the interior domain and in the layer by letting $\sigma(x)$ vanish in the interior.

2.3 Relation between PML and smooth exterior scaling

The idea of smooth exterior scaling (SES) is the same as the idea of the PML. Outgoing waves are dampened as they travel out of the interior domain by gradually increasing some absorption parameter towards the outer boundary of the layer. One way of viewing the PML method is as a complex coordinate stretch, where the real coordinate x is replaced by a complex coordinate $F(x)$ in the layer. This was first done by Chew and Weedon [12], and in this setting it becomes clear that the modal ansatz PML and the SES approaches are in fact equivalent, only written on different forms. Considering

$$F(x)=x+e^{i\gamma}\int_{x_1}^{x}\sigma(\omega)\mathrm{d}\omega,$$

as a continuation of the real coordinate x into the complex plane in the layer leads to the equation

$$i\frac{\partial u}{\partial t}=-\frac{\partial^2 u}{\partial F^2}+L\Big(y,\frac{\partial}{\partial y}\Big)u=-\frac{1}{f(x)}\frac{\partial}{\partial x}\frac{1}{f(x)}\frac{\partial u}{\partial x}+L\Big(y,\frac{\partial}{\partial y}\Big)u, \tag{2.8}$$

where

$$\frac{\mathrm{d}F(x)}{\mathrm{d}x}=f(x).$$

We note that with

$$f(x)=1+e^{i\gamma}\sigma(x),$$

(2.8) and (2.7) are identical. In SES the ansatz

$$u(x,t)=k(x)\varphi(x,t),$$

is inserted into (2.8), which for the new wave function $\varphi(x,t)$ leads to the equation

$$i\frac{\partial \varphi}{\partial t}=-\frac{1}{f(x)}\frac{\partial^2}{\partial x^2}\frac{1}{f(x)}\varphi+V_{PML}(x)\varphi+L\Big(y,\frac{\partial}{\partial y}\Big)\varphi, \tag{2.9}$$

here

$$V_{PML}(x)=\frac{\big(3f'(x)^2-2f''(x)f(x)\big)}{4f(x)^4},$$

and $k(x)$ is chosen as

$$k(x)=\frac{1}{\sqrt{f(x)}},$$

in order to eliminate the first derivatives in $\varphi(x,t)$ that appear from inserting the ansatz into (2.8).

Using (2.9) instead of (2.7) could be advantageous for more than one reason. Hermitian operators play a fundamental role in quantum mechanics. Neither the right hand side of (2.7) nor that of (2.9) are composed of a Hermitian operator operating on u. However, in a finite basis set, the operator of the right hand side of (2.9) is represented by a complex symmetric matrix H, which is not the case for (2.7). The derivation of complex coordinate scattering theory for such complex-valued Hamiltonians can be enabled through a generalized inner product called the *c-product* [10]. Another reason is that (2.9) gives a larger basis of option when choosing methods for time-propagation. An exact solution to the semi-discrete Schrödinger equation

$$i\frac{\partial \varphi}{\partial t}=H\varphi, \tag{2.10}$$

with initial conditions $\varphi(t_0)=\varphi_0$ is given at time t by

$$\varphi(t)=\varphi_0 e^{-iH(t-t_0)},$$

where H is the discretized Hamiltonian. This type of exponential expression can be used to propagate the Schrödinger equation in time. In order to avoid taking the full matrix exponential, H is commonly approximated. For instance, a few important eigenvalues and eigenvectors of H can be generated by the Lanczos algorithm, if H is a Hermitian matrix. Similar versions of the Lanczos algorithm exploiting complex symmetric structures can be applied to (2.9). However, sometimes this approach suffers from numerical instabilities [13].

2.4 Well-posedness

We consider the well-posedness of (2.9) in 1D on a finite interval with Dirichlet boundary conditions. The main result is:

Theorem 2.1. *Let*

$$\frac{1}{f}=\beta-i\alpha.$$

Assume that $\alpha\geq 0$, $\beta\geq\beta_0>0$, $\alpha,\beta\in\Re$ *and that* (2.9) *has a smooth solution in any interval* $0\leq t\leq T<\infty$. *Then*

$$||\varphi(\cdot,t)||^2_{H^p}\leq K_p(T)||\varphi(\cdot,0)||^2_{H^p},$$

$p=2m$, $m=0,1,2,\cdots,K_p$ *depends on derivatives of* f *up to order* p *for* $p\geq 2$, *and up to order* 2 *for* $p=0$, *but is uniform in* α *as* $\alpha\to 0$.

Estimates of temporal and mixed derivatives follow through the equation. Due to the uniformity of the estimates this result leads to well-posedness, since for $\alpha\geq\alpha_0>0$ the equation is parabolic and hence well-posed, see [14]. We will use this in Section 4 when we study the necessary continuity requirements of the absorption function for optimal convergence.

The restrictions of α and β corresponds to the following restriction on γ

$$0\leq\gamma\leq\frac{\pi}{2}. \tag{2.11}$$

The proof of the theorem is found in Appendix A.

3 Numerical approximations

To begin with we considered the Schrödinger equation with PML (2.7), and solved numerically in 1D using finite difference schemes of Crank-Nicolson type. Later we realized the advantages of the corresponding SES formulation (2.9) mentioned in the previous section. We also found that high order spatial discretizations are more easily derived for Eq. (2.9) than for Eq. (2.7). Therefore we used the SES formulation (2.9) for our 2D computations.

The interior domains are $[-5,5]$ in 1D and $[-3,3]\times[-5,5]$ in 2D, with PMLs starting at $x_1=5$ and $x_1=3$, respectively. Dirichlet boundary conditions are imposed on the outer boundary of the PML as well as on the other boundaries. The schemes for (2.7) are second and fourth order in space, respectively, while the schemes for (2.9) are second, fourth, sixth and eighth order in space, respectively. All the schemes are second order accurate in time. The schemes for (2.7) are presented in Section 3.1 and the schemes for (2.9) in Section 3.2.

The stability properties of the numerical schemes are good. A drawback is that the Crank Nicolson method is an implicit method and a system of equations needs to be solved in each time step.

Remark 3.1. Since the schemes are only second order accurate in time, using e.g., the eighth order in space discretization (3.7) will force us to take very small time steps to retain a high accuracy. However, higher orders will be useful in combination with a more efficient time-stepping method, and also when expanding into higher dimensions in space.

3.1 Schemes for Eq. (2.7)

For Eq. (2.7) in 1D, where

$$L\Big(y,\frac{\partial}{\partial y}\Big)\equiv 0,$$

we use finite difference schemes of Crank-Nicolson type, they are second order accurate in time and second and fourth order accurate in space, respectively. The second order method is

$$\begin{aligned} i\frac{u_j^{m+1}-u_j^m}{\Delta t}=\frac{v_j}{\Delta x^2}\Big[v_{j+\frac{1}{2}}\Big(\frac{u_{j+1}^{m+1}+u_{j+1}^m}{2}-\frac{u_j^{m+1}+u_j^m}{2}\Big)-v_{j-\frac{1}{2}}\Big(\frac{u_j^{m+1}+u_j^m}{2}\\ -\frac{u_{j-1}^{m+1}+u_{j-1}^m}{2}\Big)\Big]\equiv\tilde{D}_2\Big(\frac{u_j^{m+1}+u_j^m}{2}\Big), \end{aligned} \tag{3.1}$$

where u_j^m is the grid function with space index j and time index m. The intermediate values $v_{j+1/2}$ are calculated as the mean of $v(x_j)$ and $v(x_{j+1})$, where

$$v(x)=\big(1+e^{i\gamma}\sigma(x)\big)^{-1}. \tag{3.2}$$

The Crank-Nicolson scheme without PML

$$i\frac{u_j^{m+1}-u_j^m}{\Delta t}=\frac{1}{\Delta x^2}\Big(\frac{u_{j+1}^{m+1}-2u_j^{m+1}+u_{j-1}^{m+1}}{2}+\frac{u_{j+1}^m-2u_j^m+u_{j-1}^m}{2}\Big), \tag{3.3}$$

is unconditionally stable, hence the time step should only be restricted due to accuracy requirements.

The fourth order in space, second order in time-scheme (3.6) is obtained by first combining (3.2) and the right hand side of (2.7) and expanding

$$-v(x)\frac{\partial}{\partial x}\Big(v(x)\frac{\partial u}{\partial x}\Big)=-v(x)^2\frac{\partial^2 u}{\partial x^2}-v(x)\frac{\partial v}{\partial x}\frac{\partial u}{\partial x}. \tag{3.4}$$

The right hand side of (3.4) is then discretized using central finite differences of fourth order

$$\begin{aligned} i\frac{\partial u_j}{\partial t}=&-\frac{v_j^2}{12\Delta x^2}[-u_{j+2}+16u_{j+1}-30u_j+16u_{j-1}-u_{j-2}]\\ &-\frac{v_j v_{x,j}}{12\Delta x}[-u_{j+2}+8u_{j+1}-8u_{j-1}+u_{j-2}]\equiv\tilde{D}_4 u_j. \end{aligned} \tag{3.5}$$

Here v_j and $v_{x,j}$ are the exact function values of $v(x)$ and $v_x(x)$, respectively, in grid point j. The fourth order in space, second order in time-scheme is

$$i\frac{u_j^{m+1}-u_j^m}{\Delta t}=\tilde{D}_4\Big(\frac{u_j^{m+1}+u_j^m}{2}\Big). \tag{3.6}$$

3.2 Schemes for Eq. (2.9)

In 2D, Eq. (2.9) is discretized using the following discretization scheme

$$\begin{aligned} i\frac{\varphi_{j,k}^{m+1}-\varphi_{j,k}^m}{\Delta t}=&-\frac{1}{f_j}D_{n,j}\frac{1}{f_j}\frac{\varphi_{j,k}^{m+1}+\varphi_{j,k}^m}{2}+V_{PML,j}\frac{\varphi_{j,k}^{m+1}+\varphi_{j,k}^m}{2}\\ &-D_{n,k}\frac{\varphi_{j,k}^{m+1}+\varphi_{j,k}^m}{2}+V_k\frac{\varphi_{j,k}^{m+1}+\varphi_{j,k}^m}{2}, \end{aligned} \tag{3.7}$$

where $D_{n,j}$ and $D_{n,k}$ are standard central finite difference schemes of order n for the second derivative, operating in the x- and y-directions, respectively. n is 2,4,6 and 8, respectively. $V_{PML,j}$ is the exact value of the extra potential V_{PML}, which is only x-dependent, in grid point j in the x-direction, and V_k is the exact value of the potential V, which is only y-dependent, in grid point k in the y-direction.

For all schemes, the second order stencil is used in the grid point next to the boundary, the fourth two grid points away from the boundary etc. Since the wave packet is dampened to a large extent near the outer boundary, we do not expect this to affect the overall accuracy in the PML.

4 Error analysis

There are three contributions to the error in the spatially discrete solution on the interior domain. The first contribution is a modeling error that comes from solving (2.7) on a

truncated domain instead of the unbounded domain. The second and third contributions are due to the discretization in the layer and in the interior, respectively. We refer to them as numerical reflections and discretization errors, respectively. Note that the numerical reflections and the discretization errors constitute the total spatial numerical error, i.e., the difference between a continuous solution on the truncated domain and a semi-discrete solution on the truncated domain. However, since they display different behavior, we discuss them separately.

The modeling error decreases as the thickness of the layer increases, and goes to zero as the thickness goes to infinity. However, the numerical errors will be present, regardless of the thickness of the layer. Therefore, extending the layer after a certain point will not be meaningful in terms of the total error. Instead, we want to match the modeling error with the numerical reflections, so that neither of the errors from the PML dominate, but are of the same order. Moreover, the error level should be determined by the discretization error (errors due to the numerical scheme in the interior), so that all three error sources are of the same order.

We perform error analysis with respect to Eq. (2.7) in 1D. The modeling error is considered in Section 4.1, the numerical reflections in Section 4.2 and the discretization error in Section 4.3. Since we aim at using more efficient time-propagation methods, we do not consider the temporal error in the analysis.

4.1 Modeling error

The modeling error arises when the continuous problem (2.7) is solved on the truncated computational domain, Ω_C. Consider a point in space, which is located to the right of the compact support of the initial data, i.e., at a location with larger x-coordinate, but to the left of the PML. Laplace-transformed solutions at this location are on the form

$$\hat{u}_j(x) = A_j e^{\sqrt{-is+\kappa_j^2}(x-x_1)} + B_j e^{-\sqrt{-is+\kappa_j^2}(x-x_1)},$$

which in physical space corresponds to a left-propagating and a right-propagating wave, with coefficients A_j and B_j, respectively. We define the modeling error, $\varepsilon_1(x,t)$, as the incoming (left-propagating) wave. The solutions in the layer are

$$\begin{aligned}\hat{u}_{j,PML}(x) = &A_{j,PML}\exp\left[\sqrt{-is+\kappa_j^2}\left((x-x_1)+e^{i\gamma}\int_{x_1}^{x}\sigma(\omega)\mathrm{d}\omega\right)\right]\\ &+B_{j,PML}\exp\left[-\sqrt{-is+\kappa_j^2}\left((x-x_1)+e^{i\gamma}\int_{x_1}^{x}\sigma(\omega)\mathrm{d}\omega\right)\right],\end{aligned}$$

where continuity at $x=x_1$ implies

$$A_j = A_{j,PML}, \qquad B_j = B_{j,PML}.$$

Imposing a Dirichlet boundary condition at the outer boundary of the layer, $x=x_1+d$, gives

$$\hat{u}_{j,PML}(x_1+d)=0\Rightarrow A_j=-B_j\exp\Big[-2\sqrt{-is+\kappa_j^2}\Big(d+e^{i\gamma}\int_{x_1}^{x_1+d}\sigma(\omega)\mathrm{d}\omega\Big)\Big].$$

Clearly the magnitude of the relative modeling error in Laplace space is proportional to the quotient $|A_j|/|B_j|$. In particular

$$|\hat{\varepsilon}_1(x_1,s)|=|A_j|=\frac{|A_j|}{|B_j|}|B_j|=e^{2\delta}|B_j|, \tag{4.1a}$$

$$\delta=Re\Big(\lambda_-\Big(d+e^{i\gamma}\int_{x_1}^{x_1+d}\sigma(\omega)\mathrm{d}\omega\Big)\Big),\qquad \lambda_-=-\sqrt{-is+\kappa_j^2}. \tag{4.1b}$$

We expect the $e^{2\delta}$ to be useful for approximating the modeling error also for other values of x. We see that this quantity depends on the width of the PML, the size of the integral of $\sigma(x)$ and on the specific problem in terms of κ_j^2 and s. However, it is independent of the shape of $\sigma(x)$. If the solution is dominated by certain values of s and j, the quotient for these values gives a good estimate of the relative error.

In order to derive an approximate expression for the l_2 norm of the relative modeling error in physical space, which we denote by $\bar{\varepsilon}_1$, and later for the numerical reflections from the PML, we need to determine the dominating frequencies in a dissociative process. We assume that the solution mainly consists of the lowest mode in the y-direction and that the corresponding κ_j is small. As a model of a dissociative process consider a free particle in 1D, described by

$$\begin{cases} i\dfrac{\partial u}{\partial t}=-\dfrac{\partial^2 u}{\partial x^2}, \\ u(x,0)=e^{ikx}. \end{cases} \tag{4.2}$$

The wavenumber k is related to the speed of the particle. Fourier-transforming in time and space shows that a free particle with wavenumber k corresponds to the time-harmonic frequency

$$\omega=-k^2,$$

where ω is the dual variable in time. Thus, the solution to (4.2) is given by

$$u(x,t)=e^{ikx-ik^2t}, \tag{4.3}$$

and the corresponding solution in the layer is

$$u_{PML}(x,t)=\exp\Big[ik\Big(x+e^{i\gamma}\int_{x_1}^{x}\sigma(\omega)\mathrm{d}\omega\Big)-ik^2t\Big]. \tag{4.4}$$

The time-harmonic frequency $\omega=-k^2$ corresponds to Laplace transformation along the imaginary axis, where

$$s=-ik^2.$$

Inserting $s=-ik^2$ into

$$\lambda_-=-\sqrt{-is+\kappa_j^2},$$

with $\kappa_j=0$, yields

$$\lambda_-=-\sqrt{-i(-ik^2)}=ik. \tag{4.5}$$

For a polynomial of degree p as absorption function, we get the integral

$$\begin{aligned}\int_{x_1}^{x_1+d}\sigma(\omega)\mathrm{d}\omega&=\int_{x_1}^{x_1+d}\sigma_{\max}\Big(\frac{\omega-x_0}{d}\Big)^p\\&=\Big[\sigma_{\max}\frac{(\omega-x_1)^{(p+1)}}{(p+1)d^p}\Big]\Big|_{x_1}^{x_1+d}=\sigma_{\max}\frac{d}{p+1}.\end{aligned} \tag{4.6}$$

Inserting (4.5) and (4.6) into (4.1), yields

$$e^{2\delta}=\exp\Big(\frac{-2k\sin(\gamma)\sigma_{\max}d}{p+1}\Big). \tag{4.7}$$

In a dissociative process, where we know the dominating frequencies approximately, we expect this quantity to approximate the relative modeling error also in physical space. According to (4.7), the error can be expected to decrease exponentially as the wave number, k, the width of the PML, d, and the strength of the absorption, $\sigma_{\max}$, increase. Note that by letting $\sigma_{\max}$ depend on the degree of the polynomial, p, the value of the integral can be kept constant independently of p. This is validated by numerical results for specific initial data in Section 5.1. In [15], a study was done for more general data, which in the dissociative state was known only as a numerical solution. Here, it was demonstrated that expression (4.7) can be applied for such problems, by determining the dominating frequencies numerically via Fourier transform.

Remark 4.1. To model a particle moving with speed k initial data

$$u(x,0)=e^{-x^2+ikx},$$

is often used. Laplace-transforming equation (4.2) with this initial data in time and Fourier-transforming in space, yields

$$\hat{\tilde{u}}(\xi,s)=\frac{i\sqrt{\pi}}{is-\xi^2}e^{-\frac{(\xi-k)^2}{4}}. \tag{4.8}$$

From this expression, we see that the solution is dominated by modes near $\xi=k$ and $s=-ik^2$.

Remark 4.2. In the model problem $Re(s)=0$. If we instead consider a more general case with $s=-ik^2+\alpha_1$, we have

$$\lambda_-=-\sqrt{-i(-ik^2+\alpha_1)+\kappa_j^2}=ik_2-\alpha_2,\qquad \alpha_2>0. \tag{4.9}$$

Now consider the Laplace-transform of a rightgoing wave in the layer,

$$\hat{u}_{j,PML}(x)\approx B_j\exp\Big[\lambda_-\Big(x+e^{i\gamma}\int_{x_1}^{x}\sigma(\omega)\mathrm{d}\omega\Big)\Big]. \tag{4.10}$$

Inserting (4.9), gives

$$\hat{u}_{j,PML}(x)\approx B_j e^{(ik_2-\alpha_2)(x+\Sigma_a+i\Sigma_b)}=e^{ik_2(x+\Sigma_a)-i\alpha_2\Sigma_b}e^{-k_2\Sigma_b-\alpha_2(x+\Sigma_a)}, \tag{4.11}$$

where

$$e^{i\gamma}\int_{x_1}^{x}\sigma(\omega)\mathrm{d}\omega=\Sigma_a+i\Sigma_b.$$

Here Σ_a and Σ_b are real and positive.

Note that Σ_a corresponds to a real grid stretch, whereas Σ_b corresponds to a continuation of x into the complex plane. Here, both Σ_a and Σ_b will contribute to the dampening of the wavepacket. More specifically, Σ_b dampens outgoing traveling waves whereas Σ_a helps to dampen the solution in the layer in the presence of evanescent waves. The relation between Σ_a and Σ_b is determined by the parameter γ.

4.2 Numerical reflections from the PML

Consider (2.7) in 1D with $V\equiv 0$. Discretizing the continuous PML equation (2.7) in space introduces numerical reflections, which we denote ε_2, that depend on the truncation error inside the PML. The truncation error of the spatial part of the second order scheme (3.1) is to leading order

$$T_{\varepsilon_2,j}=-\Delta x^2 v\Big(\frac{vu_{xxxx}}{12}+\frac{v_x u_{xxx}}{6}+\frac{v_{xx}u_{xx}}{8}+\frac{v_{xxx}u_x}{24}\Big), \tag{4.12}$$

in grid point j, for grid points in the layer. Here v is given by (3.2).

Assuming that the dominating spatial frequency is k, an expression of the truncation error can be derived in terms of

$$\tilde{\sigma}(x)=e^{i\gamma}\sigma(x),$$

derivatives of $\tilde{\sigma}(x)$, spatial frequency k and the solution in the layer, $u_{PML}(x,t)$. Inserting the PML solutions from the model problem (4.4) and Eq. (3.2) into (4.12), yields

$$\begin{aligned}T_{\varepsilon_2,j}=-\Delta x^2\frac{1}{1+\tilde{\sigma}_j}\Big[&-\frac{5}{24}k^2\tilde{\sigma}_j''+\frac{1}{24}\frac{1}{(1+\tilde{\sigma}_j)}ik\tilde{\sigma}_j'''-\frac{1}{24}\frac{1}{(1+\tilde{\sigma}_j)^2}ik\tilde{\sigma}_j'\tilde{\sigma}_j''\\&-\frac{1}{3}(1+\tilde{\sigma}_j)ik^3\tilde{\sigma}_j'+\frac{1}{12}(1+\tilde{\sigma}_j)^3k^4\Big]u_{PML}(x_j,t)+\mathcal{O}(\Delta x^4).\end{aligned} \tag{4.13}$$

Then the numerical reflections in grid point j, $\varepsilon_{2,j}$, fulfills

$$i\frac{\partial \varepsilon_{2,j}}{\partial t} = D_2\varepsilon_{2,j} + T_{\varepsilon_2,j}, \tag{4.14}$$

for grid points in the whole computational domain. Note that with our definition of ε_2, the terms depending on the absorption function in $T_{\varepsilon_2,j}$ vanish at interior points. We still expect ε_2 to be non-zero in the interior, since the truncation error is transported with the error equation (4.14). We are interested in the accuracy of the solution in the interior domain.

If the numerical scheme is stable, the convergence rate is determined by the truncation error. Near the interface the second term on the right hand side in (4.13) (with the third derivative) is likely to dominate. For instance, for third order polynomials, the second term is uniformally non-zero at points near the interface, while all other sigma-dependent terms vanish. Thus, if $\sigma(x)$ is a polynomial of degree p according to (4.6), we expect the truncation error to behave like

$$\sim \frac{\sigma_{\max}}{d^p}\Delta x^2, \tag{4.15}$$

thus, we expect the relative l_2 error of the numerical reflections from the PML to behave like

$$\bar{\varepsilon}_2 \equiv \sqrt{\Delta x \sum |\varepsilon_{2,j}|^2} \approx C_2(k)\frac{\sigma_{\max}}{d^p}\Delta x^2, \tag{4.16}$$

where the sum is taken over the points in the interior. $C_2(k)$ is a numerical constant that depends on the dominating frequency. The behavior of the expression (4.16) with respect to $\sigma_{\max}$, d, p and Δx is verified by numerical experiments in Section 5.2. In Section 5.2, we also see that $\bar{\varepsilon}_2$ decreases with increasing k.

A similar study of the truncation error for the schemes (3.7) show that also here a term proportional to $\sigma_{\max}/d^p$ will always be present in the term with the highest derivative. Thus, we expect a $\sigma_{\max}/d^p$ behavior for $\bar{\varepsilon}_2$ also for the schemes (3.7), so that

$$\bar{\varepsilon}_2 \approx C_n(k)\frac{\sigma_{\max}}{d^p}\Delta x^n, \tag{4.17}$$

where n is the order of the spatial discretization. In order to obtain optimal convergence, the order of the polynomial, p, needs to be chosen sufficiently large with respect to n.

To understand this we analyze the continuous error equation corresponding to an nth order spatial approximation of (2.9) in 1D with Dirichlet boundary conditions

$$\begin{cases} i\dfrac{\partial e}{\partial t} = -\dfrac{1}{f}\dfrac{\partial^2}{\partial x^2}\Big(\dfrac{1}{f}e\Big) + V_{PML}e + \Delta x^n T_e, \\ e(x,0) = 0. \end{cases} \tag{4.18}$$

Here, n is assumed to be even and

$$T_e = \frac{c_n}{f}\frac{\partial^{n+2}}{\partial x^{n+2}}\Big(\frac{1}{f}\varphi\Big). \tag{4.19}$$

In particular, we note that $||T_e||$ is bounded if $||\varphi||_{H^{n+2}}$ and $|f^{(m)}|_\infty$, $0\leq m\leq n+2$, are bounded. Remembering Theorem 2.1, we see that this is achieved by σ being a polynomial of at least degree $n+2$. By Duhamel's principle we have by Theorem 2.1

$$||e(\cdot,t)||_2^2\leq \Delta x^n K_0(T)\int_0^t ||T_e(\cdot,\tau)||^2 \mathrm{d}\tau. \tag{4.20}$$

Thus, if σ is a polynomial of degree at least $n+2$, the integral is bounded and we are sure to have optimal convergence. This result is true for all $\alpha\geq 0$. However, in the layer the equation is of parabolic type, and less smoothness may be required there for optimal convergence. If we restrict ourselves to the layer, assuming $\alpha\geq\alpha_0>0$ we can show

Lemma 4.1. *If $\alpha\geq\alpha_0>0$ and $|\sigma^{(m)}|_\infty<\infty$ for $0\leq m\leq n+1$, then*

$$||e(\cdot,t)||_2^2\leq \Delta x^n \tilde{K}(T),$$

where $\tilde{K}(T)$ depends on $\sigma^{(m)}$, $0\leq m\leq n+1$ and $||\varphi||_{H^{n+1}}$.

The proof is found in Appendix B. Now a polynomial of order $n+1$ ensures optimal convergence (n odd). For higher order schemes we actually get optimal convergence with less smoothness in σ. A more refined analysis would be required to fully understand this behavior.

4.3 Discretization error from the interior

For the scheme in the interior, where $\tilde{\sigma}=0$, all terms but the last one in (4.13) will vanish, and the truncation error in the interior is approximately

$$T_{\varepsilon_0,j}\approx -\frac{\Delta x^2 k^4}{12}u(x_j,t). \tag{4.21}$$

For a plane wave with unit amplitude and spatial frequency k, there is an explicit expression for the pointwise error in the interior at time T

$$\varepsilon_{0,j}=\big|u(x_j,T)-u_j(T)\big|.$$

The pointwise error for the second order scheme is at most

$$\max_j\{\varepsilon_{0,j}\}=\frac{\Delta x^2 k^4}{12}T+\mathcal{O}(\Delta x^4), \tag{4.22}$$

for grid points j in the interior domain (see [17], pp. 93).

We cannot use this error bound in a strict sense here, since we do not expect plane wave solutions. However, we expect the relative l_2 norm of the discretization error from the interior domain to behave like

$$\bar{\varepsilon}_0\equiv\sqrt{\Delta x\sum|\varepsilon_{0,j}|^2}\approx C\frac{\Delta x^2 k^4}{12}T. \tag{4.23}$$

Numerical tests presented in Section 5 show that (4.23) gives a good estimation of the l_2 norm of the discretization error from the interior and that the proportionality constant $C \approx 1$. This is not surprising since the l_2 norm of the solution is of order unity. For general initial data, we refer to the error estimate (4.20) in the previous section.

4.4 Matching of errors

Making the requirement that the l_2 error of the numerical reflections, $\bar{\varepsilon}_2$, should not amount to more than ten percent of the l_2 error of the discretization error from the interior, $\bar{\varepsilon}_0$, yields

$$C_2(k)\frac{\sigma_{\max}}{d^p}\Delta x^2 \leq 0.1 C_0(k,T)\Delta x^2,$$

where

$$C_0(k,T) = C\frac{k^4 T}{12}.$$

We define M as

$$M = \frac{\sigma_{\max}}{d^p}, \tag{4.24}$$

which gives

$$C_2(k) M \Delta x^2 \leq 0.1 C_0(k,T)\Delta x^2. \tag{4.25}$$

The constants $C_2(k)$ and $C_0(k,T)$ can be determined numerically and we get the largest possible value of M from (4.25)

$$M = \frac{0.1 C_0(k,T)}{C_2(k)}. \tag{4.26}$$

At the same time, we require that the relative modeling error from the PML, $\bar{\varepsilon}_1$, should not exceed ten percent of $\bar{\varepsilon}_0$, i.e.,

$$\exp\Big[\frac{-2k\sin(\gamma)\sigma_{\max} d}{p+1}\Big] \leq 0.1 C_0(k,T)\Delta x^2. \tag{4.27}$$

Here we have used the approximation (4.7). By inserting (4.24) into (4.27), the smallest possible value of d can be determined as

$$d = \sqrt[p+1]{\frac{-ln\big(0.1 C_0(k,T)\Delta x^2\big)(p+1)}{2k\sin(\gamma) M}}, \tag{4.28}$$

and the corresponding $\sigma_{\max}$ is determined from (4.24).

5 Numerical experiments

Numerical experiments are performed in both 1D and 2D. In 1D, we perform numerical experiments with a zero potential and verify that the behavior of the modeling error agrees with our theoretical formulas. We show that the numerical reflections go to zero at the expected rate as the mesh is refined for the second and fourth order in space schemes, (3.1) and (3.6). Also, we investigate how the numerical reflections from the PML depend on the layer parameters and how to choose parameters so that the different types of errors are matched. An interesting observation is that when the PML is sufficiently wide and the absorption function is smooth, the numerical reflections from the PML, ε_2, is often the least significant error as the wave packet is sufficiently resolved. For those grids, coarser grids actually perform slightly better, which likely is due to the fact that finer grids succeed in transporting the error more efficiently.

The model problem (4.2) with initial data $u(x,0)=e^{-x^2+ikx}$ has in the absence of boundaries the exact solution

$$u_{exact}(x,t)=\sqrt{\frac{i}{-4t+i}}\exp\Big(\frac{-ix^2-kx+k^2t}{-4t+i}\Big).$$

We solve (2.7) in 1D and compare the numerical solution, u_{PML}, to the exact solution, u_{exact}, and to a reference solution, u_{ref}. u_{ref} is calculated on the same grid as u_{PML} but without PML and on a larger domain. The reference solution is used in order to be able to distinguish between the numerical reflections from the PML, ε_2, and the discretization error of the interior scheme, ε_0. The l_2 error with respect to the exact solution is calculated at time T as

$$\frac{||u_{PML}(\cdot,T)-u_{exact}(\cdot,T)||_2}{||u_{exact}(\cdot,0)||_2}, \tag{5.1}$$

where

$$||u(\cdot,t)||_2=\Big(\Delta x\sum_i|u(x_i,t)|^2\Big)^{\frac{1}{2}}.$$

The sums are taken only over points in the interior domain. The l_2-error with respect to the reference solution is calculated correspondingly. As absorption functions, we use polynomials of degree p, on the form

$$\sigma(x)=\sigma_{\max}\Big(\frac{x-x_0}{d}\Big)^p,$$

with $p\geq 4$.

5.1 Modeling error

We expect the l_2 norm of the modeling error, $\bar{\varepsilon}_1$, to decrease exponentially with respect to wave number k, the strength of the absorption function $\sigma_{\max}$, and the width of the PML d,

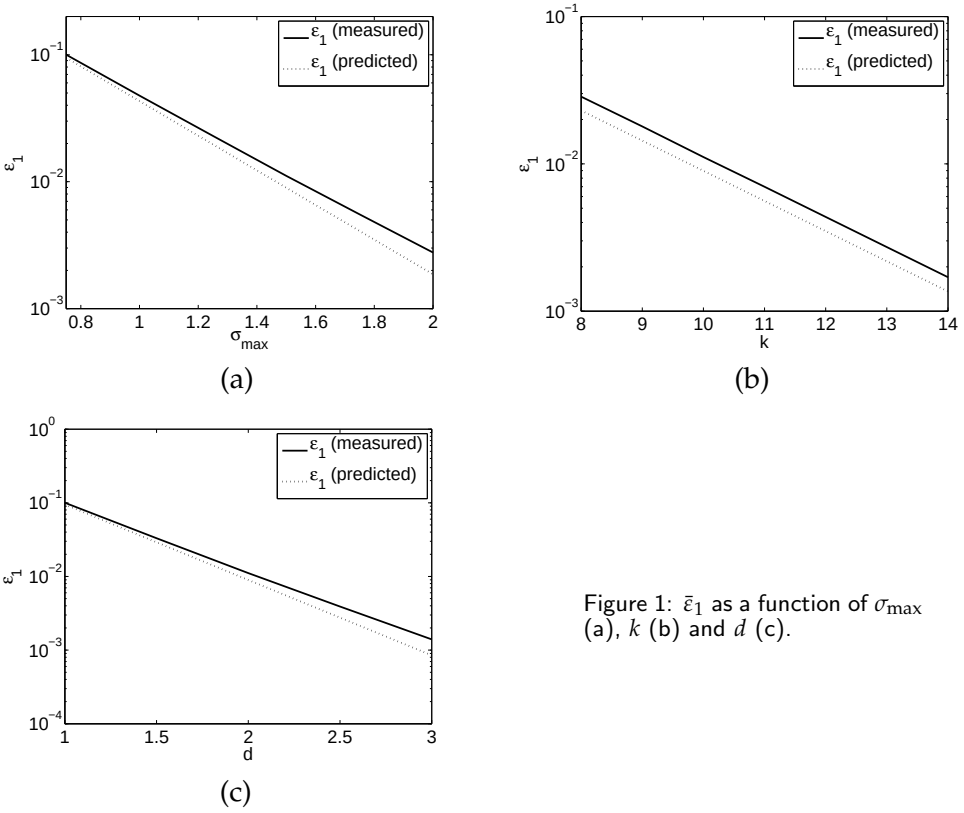

Figure 1: $\bar{\varepsilon}_1$ as a function of $\sigma_{\max}$ (a), k (b) and d (c).

see (4.7). This behavior is verified and displayed in Fig. 1. We use (3.1) with $\Delta x = 1\times 10^{-3}$, $\Delta t = 1\times 10^{-4}$ on the domain $x = [-5,7]$, where the interior domain is $x = [-5,5]$ and the PML starts at $x_1 = 5$. The simulations are run until $T = 1$. We also see from Fig. 1 that the predicted modeling error agrees with the measured. An eighth order polynomial is used as absorption function with relatively low values of $\sigma_{\max}$ to ensure that the numerical reflections are small and the modeling error is dominating. $\sigma_{\max}$, k and d are varied separately, elsewhere we have $\sigma_{\max} = 1.5$, $k = 10$, $d = 2$ and $\gamma = \pi/4$.

From the results displayed in Fig. 1, we conclude that the behavior of the modeling error is in agreement with the theory in Section 4.1 and that (4.7) gives an estimate of the modeling error also in physical space.

5.2 Numerical reflections

We expect the l_2 error of the numerical reflections from the PML, $\bar{\varepsilon}_2$, to behave as in (4.17). It should increase linearly with respect to $\sigma_{\max}$ and depend on the width of the PML, d, as d^{-p}, where p is the order of the polynomial used. We investigate the behavior of the numerical reflections with respect to Δx and $\sigma_{\max}$, for a constant shape of the absorption function. We use a wide PML with $d = 4$ to ensure that the modeling error is kept small

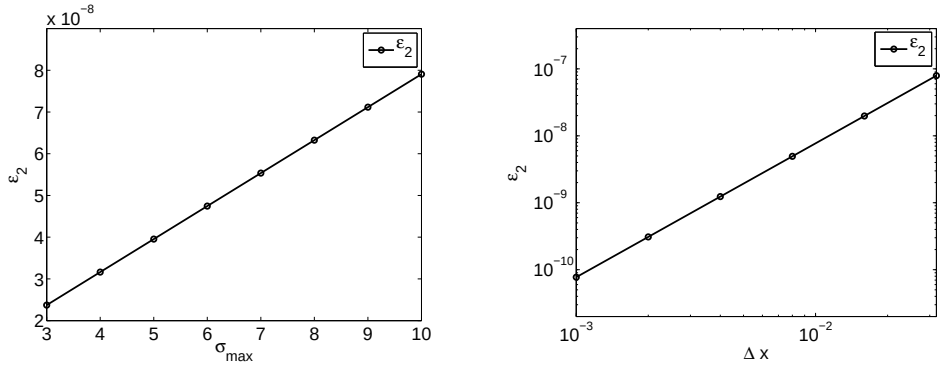

Figure 2: $\bar{\varepsilon}_2$ as a function of $\sigma_{\max}$ (a) and Δx (b).

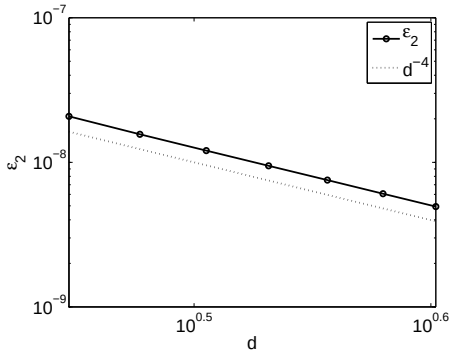

Figure 3: $\bar{\varepsilon}_2$ as a function of d, logarithmic scale.

and the numerical reflections from the interface of the PML are dominating. The grid size as well as $\sigma_{\max}$ are varied in order to investigate the behavior of the numerical reflections from the PML using (3.1). First, we keep the grid fixed with $\Delta x = 3.2\times 10^{-2}$ and we use $\Delta t = 10^{-4}$ and a 4th order polynomial. Other constants are $k=10$, $d=4$, $\gamma=\pi/4$. The simulations are run until $T=1$. In Fig. 2, we see the linear and quadratic behaviors of $\bar{\varepsilon}_2$ with respect to $\sigma_{\max}$ and Δx, respectively. These simulations are run until $T=0.1$.

In Fig. 3, we see how $\bar{\varepsilon}_2$ depends of the width, d. Here we use $\Delta x = 8\times 10^{-3}$, $\Delta t = 10^{-4}$, $\sigma_{\max}=10$, $p=4$ and vary d. The slope in Fig. 3 is determined to -4.02, clearly showing a d^{-p}-behavior as expected.

In Table 1, $\Delta x = 8\times 10^{-3}$ is kept and k is varied. We use $d=4$, $\sigma_{\max}=10$, $\Delta t = 10^{-4}$ and $\gamma=\pi/4$. The numerical reflections from the interface decrease as k increases, which is not what we would expect by looking at the truncation error. However, we have seen that the performance of the PML increases vastly for higher frequencies and this is likely an effect of that. For comparison, we have included values of the l_2 error of the discretization error in the interior, $\bar{\varepsilon}_0$, obtained from (4.23) and by direct measurement from numerical

Table 1: Discretization error with varying k.

k	$\bar{\varepsilon}_2$ (measured)	$\bar{\varepsilon}_0$ (measured)	$\bar{\varepsilon}_0$ (predicted)
8	7.9900×10^{-9}	5.9853×10^{-3}	5.3084×10^{-3}
9	6.1823×10^{-9}	8.4365×10^{-3}	7.6982×10^{-3}
10	4.9414×10^{-9}	1.1510×10^{-2}	1.0773×10^{-2}
11	4.0448×10^{-9}	1.5281×10^{-2}	1.4523×10^{-2}
12	3.3745×10^{-9}	1.9828×10^{-2}	1.9021×10^{-2}
13	2.8596×10^{-9}	2.5232×10^{-2}	2.4372×10^{-2}
14	2.4550×10^{-9}	3.1581×10^{-2}	3.0732×10^{-2}

experiments in the same table. We see from Table 1 that the measured values agree with the predicted values.

The measured values of $\bar{\varepsilon}_0$ are computed by comparison with the exact solution at the time when the wavepacket starts to enter the PML, at $t=0.202$. After this time the measured error decreases since the solution is leaving the interior domain. The predicted values are computed using formula (4.23) at the same time, with $C=1$. $\bar{\varepsilon}_2$ is computed with respect to the reference solution, so that only the PML error is taken into account. Moreover, due to the wide PML, we expect $\bar{\varepsilon}_1$ to be negligible.

In Fig. 4, we see the l_2-error of a numerical solution compared to a reference solution as a function of time, and thus, the error displayed stems from the PML. In (a) and (b), the solution is computed using (3.1) and in (c) and (d) (3.6) is used. Fig. 4 (b) and (d) are close ups displaying parts of Fig. 4 (a) and (c), respectively. The computations are run for three different discretizations, with consecutively halved step lengths, $\Delta x=4\times10^{-2}$, 2×10^{-2}, and 1×10^{-2}, corresponding to the blue, red and green lines in the figures, respectively. The wave enters the PML before $t=0.2$ causing numerical reflections and after $t=0.7$ the modeling error appears. The total simulation time is $T=1.5$. We see in Fig. 4 (a) that the modeling error for the finest discretization is of the same size as the modeling error for all discretizations in Fig. 4 (c), but for coarser grids this error is smaller. This is likely due to the fact that for coarser grids information is lost when the wave propagates. Here we have used parameter values

$$k=10,\quad p=8,\quad d=4,\quad \sigma_{\max}=\frac{9}{4},\quad \gamma=\frac{\pi}{4},$$

and the time-step $\Delta t=10^{-5}$.

The l_2 error of the numerical reflections from the interface are converging for the 2nd order discretization, while for the 4th order discretization they are already of the order of roundoff, as we see in Fig. 4. The l_2 error of the discretization error in the interior (where $\sigma(x)=0$) converges with 2nd and 4th order respectively, see Fig. 5.

Worth to note is that for well resolved wave packets the discretization error from the interior is dominating compared to the numerical reflections from the interface of the PML.

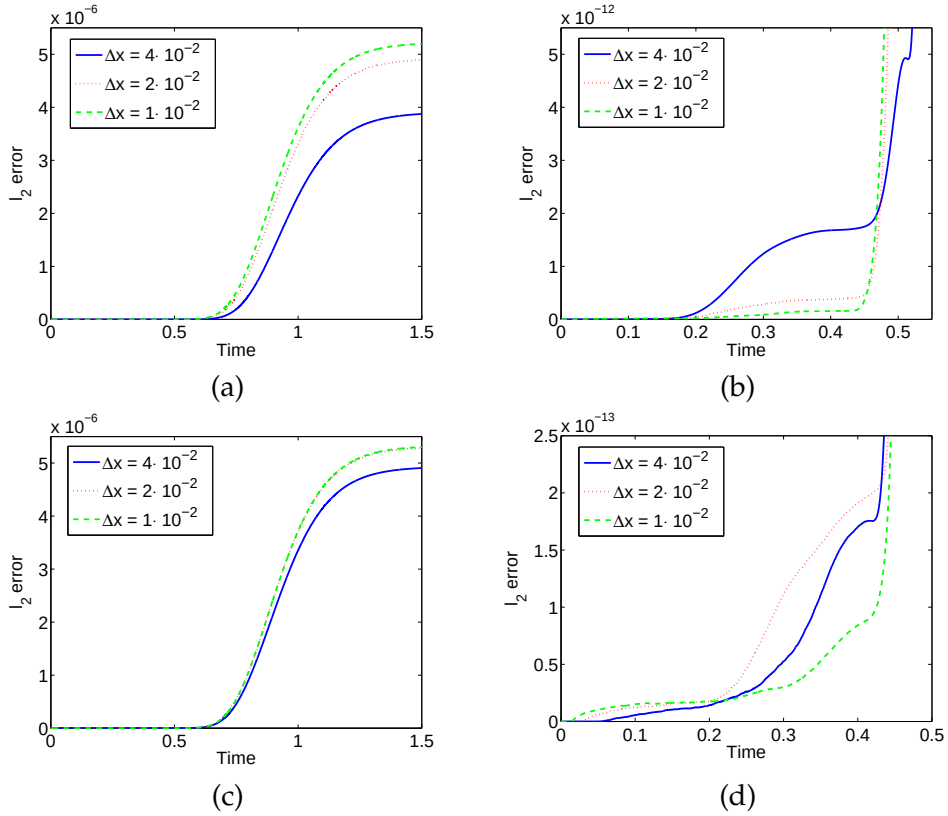

Figure 4: PML error as a function of time. 2nd order (a), 2nd order zoom (b), 4th order (c), 4th order zoom (d).

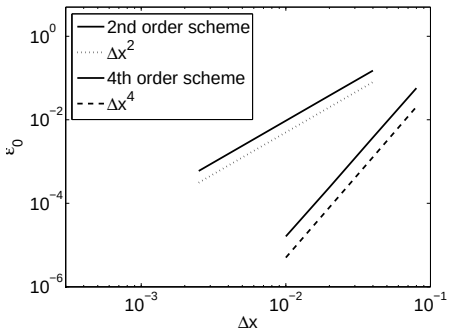

Figure 5: Grid convergence of 2nd and 4th order schemes.

5.3 Matching of errors

We want to match the errors from the PML so that they are of the same order, where the magnitude is determined from the magnitude of the discretization error in the interior. Increasing $\sigma_{\max}$ makes the modeling error decrease, while the numerical reflections

increase. An alternative way of decreasing the modeling error is to increase d, and this also decreases the numerical reflections from the PML. We match d and $\sigma_{\max}$ for a fixed PML profile following the procedure described in Section 4.4, so that a minimal number of points can be used in the PML for a given level of accuracy.

We measure $\bar{\varepsilon}_0$ and use it as error level. $C_2(k)$ is numerically determined to be $C_2(10)\approx 4.9\times 10^{-4}$, for $p=4$. We continue by determining M from (4.26), d from (4.28) and $\sigma_{\max}$ from (4.24). The results obtained when using the optimized values are displayed in Table 2.

Table 2: Matching errors with varying Δx.

Δx	$\bar{\varepsilon}_0$	d	$\sigma_{\max}$	$\bar{\varepsilon}_m$ (measured)	$\%\bar{\varepsilon}_0$
3.2×10^{-2}	1.8246×10^{-1}	0.192	12.25	2.3910×10^{-2}	13.10
1.6×10^{-2}	4.5533×10^{-2}	0.192	12.23	8.7667×10^{-3}	19.27
8×10^{-3}	1.1509×10^{-2}	0.192	12.37	3.2230×10^{-3}	28.00
4×10^{-3}	3.0248×10^{-3}	0.196	14.12	8.7576×10^{-4}	28.95
2×10^{-3}	9.0628×10^{-4}	0.196	16.92	2.0179×10^{-4}	22.27
1×10^{-3}	3.7770×10^{-4}	0.180	20.07	1.0079×10^{-4}	26.69

When we cannot choose the exact width due to the grid size, we choose to use one extra gridpoint. This improves the result significantly compared to using one gridpoint less. The total measured error from the PML, denoted $\bar{\varepsilon}_m$, and the relation between $\bar{\varepsilon}_m$ and $\bar{\varepsilon}_0$ is also presented in Table 2. We have prescribed that the total error from the PML should be 20 percent or less, and we see that we get a slightly larger error from the PML than that. However, it does not exceed 30 percent of the interior error. Also, note that the width of the PML almost can be kept constant and the error is still reduced by increasing $\sigma_{\max}$. The width d here amounts to less than a third of the de Broglie wavelength of the dominating frequency of the wave packet.

6 2D experiments

In the 2D experiments, we use the complex symmetric schemes (3.7) on the interior domain $[-3,3]\times[-5,5]$ with a PML placed in the positive x-direction, starting at $x_1=3$. Dirichlet boundary conditions are posed both in the y-direction and at $x_0=-3$. We solve (2.9) with

$$L\Big(y,\frac{\partial}{\partial y}\Big)=-\frac{\partial^2}{\partial y^2}+V,$$

and initial condition

$$u_0(x,y)=\exp\Big[-(x-x_0)^2+ik_x(x-x_0)-(y-y_0)^2+ik_y(y-y_0)\Big],$$

where $k=10$, $k_x=k\cdot\cos\theta$ and $k_y=k\cdot\sin\theta$, and θ is the angle of direction of the gaussian pulse with respect to the x-axis. x_0 and y_0 are chosen so that the pulse reaches the PML

at a specific time $\tilde{t}$ independent of θ. We use the time step $\Delta t = 0.01$ and run until time $T = 0.6$. Both a constant potential V, and a potential $V = V(y)$ are used. For illustrative purposes, we also use $V = V(x,y)$. Optimal PML parameters derived in 1D are used, see Table 3.

Table 3: PML errors in 1D and 2D for optimal parameters.

order	Δx	d (points)	$\sigma_{\max}$	1D error	2D error
4	5×10^{-2}	0.55 (11)	6.03	4.71×10^{-4}	4.71×10^{-4}

6.1 Zero potential

In the zero potential case, where

$$L\Big(y,\frac{\partial}{\partial y}\Big) = -\frac{\partial^2}{\partial y^2},$$

the exact solution to the two-dimensional model problem with initial data from Section 6 is given by

$$u_{exact}(x,y,t) = \frac{i}{-4t+i}\exp\Big[\frac{-i(x-x_0)^2-k_x(x-x_0)+k_xt^2-i(y-y_0)^2-k_y(y-y_0)+k_yt^2}{-4t+i}\Big].$$

As in the 1D case, the l_2 error is computed over the interior points with (5.1). Here

$$||u(x,y,t)||_2 = \Big(\Delta x\Delta y\sum_i\sum_j|u(x_i,y_j,t)|^2\Big)^{\frac{1}{2}}.$$

The 2D computations yield the same results as the 1D computations, if the pulse enters the PML in the normal direction. This is displayed in Table 3. If the incoming pulse enters the PML with some other angle, the damping decreases somewhat with increasing angle, see Table 4. Here, the optimal parameters from the case with spatial discretization of order 4 and $\Delta x = 0.05$ are used. Only the angle of the pulse is varied. We have also performed the same experiments with spatial discretization of order 6 and 8. However, the memory requirements for Matlab put a restriction on the largest possible number of grid points in the computations. The results from computations using this grid size are for the 6th and 8th order schemes not in the asymptotic region of the asymptotic error formulas (4.17) and (4.23). We can therefore not expect them to display asymptotic behavior. In fact, for these experiments the damping increases somewhat with increasing angle.

In order to convince that the parameters from Table 3 in fact are optimal Fig. 6 displays the errors that arise using the same profile, but extending the PML with some extra points. We see that the error decreases to some extent, but then flattens out due to the

Table 4: PML error with varying incoming angle.

θ	$\bar{\varepsilon}_m$
0	4.71×10^{-4}
5 ($\pi/36$)	4.78×10^{-4}
10 ($\pi/18$)	4.98×10^{-4}
15 ($\pi/12$)	5.32×10^{-4}
20 ($\pi/9$)	5.81×10^{-4}
25 ($5\pi/36$)	6.41×10^{-4}
30 ($\pi/6$)	7.10×10^{-4}
35 ($7\pi/36$)	8.04×10^{-4}
40 ($2\pi/9$)	1.04×10^{-3}
45 ($\pi/4$)	2.10×10^{-3}

dominating numerical reflections. Hence, using a wider PML at this point only gives a higher cost but no gain in accuracy. Moreover, halfing the step length when d=0.55 yields the error 1.63×10^{-4}, i.e., the error is reduced, but far from reduced with 4th order convergence rate. This is due to the fact that while the numerical reflections converge with 4th order convergence rate when refining the grid, the modeling error in not reduced with grid-refinement. The balance between the two error sources implies that the parameters are optimal for the 4th order method with $\Delta x=0.05$.

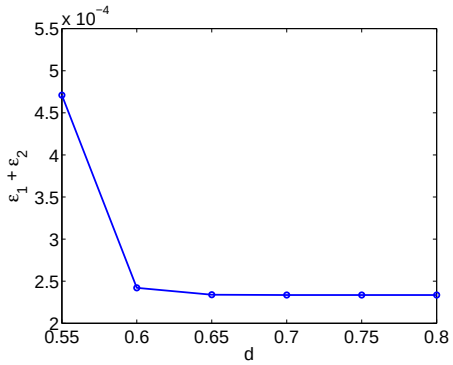

Figure 6: l_2-error as a function of d for a fixed absorption profile.

6.2 Harmonic oscillator potential

As we have seen for the zero potential case, the angle of the incoming wave does not significantly affect the absorption properties. However, when a potential channel is considered, the alignment of the potential is of importance. We perform experiments with a harmonic oscillator potential channel to illustrate this. Here

$$V(x,y)=30\big(y-x\cdot\tan(\theta)\big)^2,$$

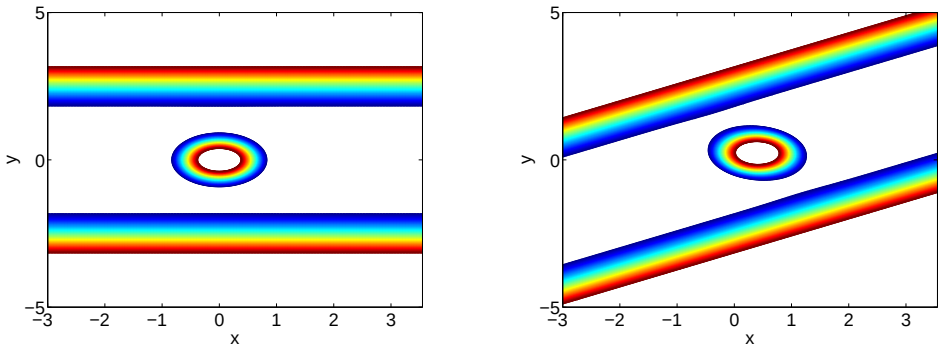

Figure 7: Gaussian pulse in potential channel aligned with x-axis (a) and channel dependent on both x and y (b).

where θ is the angle with which the potential channel is rotated from the x-axis. In the case of an "aligned" channel, $\theta=0$, so that $V=V(y)=30y^2$, and thus independent of the x-direction, see Fig. 7 (a). For a "skewed" channel, $\theta\neq 0$, and $V=V(x,y)$ is thus dependent of both x and y, see Fig. 7 (b). Initial data is suitably scaled and depicted together with the potential in the contour plots in Fig. 7.

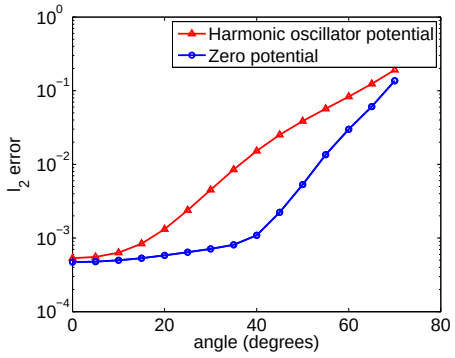

Figure 8: PML error as a function of angle θ.

In Fig. 8, we see how the reflections from the PML are affected by rotating the channel with an angle θ from the x-axis (red line with triangles). For all computations, the pulse travels in alignment with the channel and starts at the same distance from the PML interface. For comparison we have plotted the results for the zero potential case for different incoming angles (blue line with circles) in the same figure. In both sets of experiments, the numerical solution is compared to a reference solution. We see that the effectiveness of the absorption of the PML is clearly reduced when the angle between the potential and the x-axis is increased. This is not surprising, since the PML derivation is based on alignment of the potential channel with the normal direction of the layer, in this case the

x-axis. Hence, aligning the potential channels with the computational grid is desirable. The effectiveness is affected also for the zero potential case, but not at all to the same extent if the angle of the incoming wave is smaller than around $\pi/4$. As the angle is increased over $\pi/4$, the performance of the PML deteriorates. For glancing waves, the absorption in the zero potential case is only marginally better than for the skewed potential. Although, the PML is perfectly matched for all incoming angles the absorption properties of the PML are impaired as the angle increases. We refer to [8] for details on this matter.

7 Conclusions

Our approximate error formulas describe qualitative behavior of the error with respect to strength of damping, thickness of the layer and grid size, which enables optimization of the PML. Numerical experiments show that by using our formulas it is possible to match the error due to numerical reflections and the modeling error of the PML, so that the layer performs with a prescribed accuracy, as seen in Table 2. Lowering the error tolerance calls for increased strength in the absorption parameter, but the width of the layer can be kept constant, here constituting of less than a third of the de Broglie wavelength corresponding to the dominating frequency for the zero potential case.

Also, the optimized PML parameters give similar results in 2D. When the wave packet is traveling in a potential channel, we show that the alignment of the potential channel with the coordinate axis, in which the PML is placed is important, especially for angles up to $\pi/4$. Reducing the alignment results in increased numerical reflections and therefore alignment of the computational grid and the potential channel is desirable.

Appendix A

In this appendix, estimates of the solution to Eq. (2.9) in 1D, $\varphi(x,t)$, and its derivatives are derived. Dirichlet boundary conditions are assumed. The calculations are carried out using techniques from [14]. Eq. (2.9) in 1D with the substitution $v=1/f$ is

$$i\varphi_t = -v(v\varphi)_{xx} + V_{PML}\varphi, \tag{A.1}$$

where

$$V_{PML} = \frac{2vv_{xx} - v_x^2}{4}. \tag{A.2}$$

We get

$$\begin{aligned}\frac{\partial}{\partial t}||\varphi||^2 &= \int \varphi^*\varphi_t + \varphi_t^*\varphi \\ &= \int i\big(v\varphi^*\big)\big(v\varphi\big)_{xx} - i\big(v^*\varphi\big)\big(v^*\varphi^*\big)_{xx} + i\big(V_{PML}^* - V_{PML}\big)\varphi^*\varphi.\end{aligned}$$

For $0\leq\gamma\leq\pi/2$, we have

$$\Re v=\beta\geq\beta_0>0,\qquad \Im v=-\alpha\leq 0.$$

Then

$$\begin{aligned}I&=\int i\left(v\varphi^*\right)\left(v\varphi\right)_{xx}-i\left(v^*\varphi\right)\left(v^*\varphi^*\right)_{xx}\\&=\int -i\left(\varphi^*(\beta-i\alpha)\right)_x\left(\varphi(\beta-i\alpha)\right)_x+i\left(\varphi(\beta+i\alpha)\right)_x\left(\varphi^*(\beta+i\alpha)\right)_x\\&=-2\int(\alpha\varphi^*)_x(\beta\varphi)_x+(\beta\varphi^*)_x(\alpha\varphi)_x.\end{aligned}$$

Denote $\varphi=z+iw$. Then

$$\begin{aligned}I&=-2\int(\alpha(z-iw))_x\left(\beta(z+iw)\right)_x+\left(\beta(z-iw)\right)_x\left(\alpha(z+iw)\right)_x\\&=-4\int(\beta z)_x(\alpha z)_x+(\beta w)_x(\alpha w)_x\\&=-4\int\alpha\beta\left(|z_x|^2+|w_x|^2\right)-4\int(\alpha_x\beta+\alpha\beta_x)(zz_x+ww_x)-4\int\alpha_x\beta_x\left(|z|^2+|w|^2\right)\\&=-4\int\alpha\beta\left(|z_x|^2+|w_x|^2\right)+4\int\left(\frac{(\alpha\beta)_{xx}}{2}-\alpha_x\beta_x\right)\left(|z|^2+|w|^2\right)\leq C_1||\varphi||^2,\end{aligned}\tag{A.3}$$

where

$$C_1=\max_x 4\left\{\frac{(\alpha\beta)_{xx}}{2}-\alpha_x\beta_x\right\},$$

$I\in\Re$, since $\alpha,\beta\in\Re$. From (A.2), we get that

$$i\left(V_{PML}^*-V_{PML}\right)=2\Im V_{PML}=\alpha_x\beta_x-\beta\alpha_{xx}-\alpha\beta_{xx}.\tag{A.4}$$

Hence,

$$\frac{\partial}{\partial t}||\varphi||^2\leq C_2||\varphi||^2,$$

where

$$C_2=\max_x\left\{(\alpha\beta)_{xx}-\alpha_x\beta_x\right\},$$

in any interval $0\leq t\leq T$, where we get the estimate

$$||\varphi(\cdot,t)||^2\leq K_0(T)||\varphi(\cdot,0)||^2,\tag{A.5}$$

where

$$K_0(T)=e^{C_2T}.$$

Substituting $w=\varphi_t$ and carrying out the above calculation for w, yields the corresponding estimate for $||\varphi_t||$

$$||\varphi_t(\cdot,t)||^2 \leq K_0(T)||\varphi_t(\cdot,0)||^2. \tag{A.6}$$

This procedure can be continued for derivatives in t of higher orders, all bounded by $K_0(T)$. Note that the time derivatives of the initial data can be estimated by spatial derivatives of the initial data up to double order. Coefficients will depend on double order derivatives of f.

The bound of $||\varphi_{xx}||$ is obtained through Eq. (A.1). Solving for φ_{xx} gives

$$\varphi_{xx} = \frac{-i}{v^2}\varphi_t - \frac{2v_x}{v}\varphi_x + \frac{V_{PML}-vv_{xx}}{v^2}\varphi,$$

and from (A.2), we get

$$||\varphi_{xx}|| \leq \frac{1}{\beta_0^2}||\varphi_t|| + \frac{2|\beta_x - i\alpha_x|_\infty}{\beta_0}||\varphi_x|| + C||\varphi||, \tag{A.7}$$

where

$$C = \frac{1}{4\beta_0^2}\left|2(\beta - i\alpha)(\beta_{xx} - i\alpha_{xx}) + (\beta_x - i\alpha_x)^2\right|_\infty.$$

By Lemma A.3.1 in [14], we have

$$||\varphi_x|| \leq \xi||\varphi|| + \frac{1}{\xi}||\varphi_{xx}||, \tag{A.8}$$

where $\xi > 0$. Inserting (A.8) into (A.7) and choosing $\xi = 4|\beta_x - i\alpha_x|_\infty/\beta_0$ yields

$$||\varphi_{xx}|| \leq C_3||\varphi_t|| + C_4||\varphi||, \quad \text{for } 0 \leq t \leq T,$$

where

$$C_3 = \frac{2}{\beta_0^2}, \qquad C_4 = \max_x\left\{\frac{2C\beta_0 + 4|\beta_x - i\alpha_x|_\infty^2}{\beta_0}\right\}. \tag{A.9}$$

Thus,

$$||\varphi_{xx}(\cdot,t)|| \leq C_3K_0(T)||\varphi_t(\cdot,0)|| + C_4K_0(T)||\varphi(\cdot,0)||. \tag{A.10}$$

(A.8) yields

$$||\varphi_x|| \leq \frac{C_3}{\xi}||\varphi_t|| + \left\{\xi + \frac{C_4}{\xi}\right\}||\varphi||, \quad \text{for } 0 \leq t \leq T,$$

so that

$$||\varphi_x(\cdot,t)|| \leq \frac{1}{2\beta_0|\beta_x - i\alpha_x|_\infty^2} K_0(T)||\varphi_t(\cdot,0)|| + \max_x \left\{ \frac{C\beta_0^2 + (8+2\beta_0)|\beta_x - i\alpha_x|_\infty^2}{2\beta_0|\beta_x - i\alpha_x|_\infty^2} \right\} K_0(T)||\varphi(\cdot,0)||. \tag{A.11}$$

Differentiating (A.1) with respect to t, yields

$$\begin{aligned} i\varphi_{tt} &= -v(v\varphi_t)_{xx} + \frac{2vv_{xx} - v_x^2}{4}\varphi_t \\ &= -v(v_{xx}\varphi_t + 2v_x\varphi_{xt} + v\varphi_{xxt}) + \frac{2vv_{xx} - v_x^2}{4}\varphi_t. \end{aligned}$$

We rearrange, so that

$$\varphi_{xxt} = \frac{-i}{v^2}\varphi_{tt} - \frac{2v_x}{v}\varphi_{xt} + \frac{-2vv_{xx} - v_x^2}{4v^2}\varphi_t,$$

which gives the estimate

$$\begin{aligned} ||\varphi_{xxt}|| \leq \frac{1}{\beta_0^2}||\varphi_{tt}|| + \frac{2}{\beta_0}|\beta_x - i\alpha_x|_\infty||\varphi_{xt}|| \\ + \frac{1}{4\beta_0^2}|2(\beta - i\alpha)(\beta_{xx} - i\alpha_{xx}) + (\beta_x - i\alpha_x)^2|_\infty||\varphi_t||. \end{aligned}$$

By Lemma A.3.1 in [14], we get

$$||\varphi_{xt}|| \leq \xi||\varphi_t|| + \frac{1}{\xi}||\varphi_{xxt}||,$$

where we choose $\xi = 4|\beta_x - i\alpha_x|_\infty/\beta_0$ so that we get the bound

$$||\varphi_{xxt}|| \leq C_3||\varphi_{tt}|| + C_4||\varphi_t||, \quad \text{for } 0 \leq t \leq T,$$

where C_3 and C_4 are specified in (A.9). Thus we get

$$||\varphi_{xxt}(\cdot,t)|| \leq C_3K_0(T)||\varphi_{tt}(\cdot,0)|| + C_4K_0(T)||\varphi_t(\cdot,0)||, \tag{A.12}$$

$$||\varphi_{xt}(\cdot,t)|| \leq \frac{1}{2\beta_0|\beta_x - i\alpha_x|_\infty^2} K_0(T)||\varphi_{tt}(\cdot,0)|| + \max_x \left\{ \frac{C\beta_0^2 + (8+2\beta_0)|\beta_x - i\alpha_x|_\infty^2}{2\beta_0|\beta_x - i\alpha_x|_\infty^2} \right\} K_0(T)||\varphi_t(\cdot,0)||. \tag{A.13}$$

If we instead differentiate (A.1) with respect to x, we get

$$\begin{aligned} i\varphi_{xt} &= \left(-v(v\varphi)_{xx} + \frac{2vv_{xx} - v_x^2}{4}\varphi \right)_x \\ &= -v_x(v\varphi)_{xx} - v(v_{xxx}\varphi + 3v_{xx}\varphi_x + 3v_x\varphi_{xx} + v\varphi_{xxx}) + \frac{vv_{xxx}}{2}\varphi + \frac{2vv_{xx} - v_x^2}{4}\varphi_x, \end{aligned}$$

so that

$$\varphi_{xt}=iv^2\varphi_{xxx}+4ivv_x\varphi_{xx}+\left(3ivv_{xx}+2iv_x^2-i\frac{2vv_{xx}-v_x^2}{4}\right)\varphi_x+\left(iv_xv_{xx}+i\frac{1}{2}vv_{xxx}\right)\varphi.$$

We rearrange and obtain a bound for $||\varphi_{xxx}||$

$$\begin{aligned}||\varphi_{xxx}||\leq&\frac{1}{\beta_0^2}||\varphi_{xt}||+\frac{4}{\beta_0}|\beta_x-i\alpha_x|_\infty||\varphi_{xx}||\\&+\frac{1}{4\beta_0^2}\left|10(\beta-i\alpha)(\beta_{xx}-i\alpha_{xx})+9(\beta_x-i\alpha_x)^2\right|_\infty||\varphi_x||\\&+\frac{1}{2\beta_0^2}\left|2(\beta_x-i\alpha_x)(\beta_{xx}-i\alpha_{xx})+(\beta-i\alpha)(\beta_{xxx}-i\alpha_{xxx})\right|_\infty||\varphi||,\end{aligned}$$

since $||\varphi_{xt}||$, $||\varphi_{xx}||$, $||\varphi_x||$ and $||\varphi||$ are all bounded. Note that the bounds for $||\varphi_{xx}||$, $||\varphi_x||$ and $||\varphi||$ all depend on $|f^{(2)}|_\infty$. The bound for $||\varphi_{xxx}||$ depends explicitly on $|f^{(3)}|_\infty$. Differentiating the equation again with respect to x and rearranging the resulting equation gives us a bound of $||\varphi_{xxxx}||$:

$$\begin{aligned}||\varphi_{xxxx}||\leq&\frac{1}{\beta_0^2}||\varphi_{xxt}||+\frac{6}{\beta_0}|\beta_x-i\alpha_x|_\infty||\varphi_{xxx}||+\frac{1}{4\beta_0^2}\left|26(\beta-i\alpha)(\beta_{xx}-i\alpha_{xx})+25(\beta_x-i\alpha_x)^2\right|_\infty||\varphi_{xx}||\\&+\frac{8}{\beta_0^2}\left|(\beta_x-i\alpha_x)(\beta_{xx}-i\alpha_{xx})+3(\beta-i\alpha)(\beta_{xxx}-i\alpha_{xxx})\right|_\infty||\varphi_x||\\&+\frac{1}{2\beta_0^2}|2(\beta_{xx}-i\alpha_{xx})^2+3(\beta_x-i\alpha_x)(\beta_{xxx}-i\alpha_{xxx})+(\beta-i\alpha)(\beta_{xxxx}-i\alpha_{xxxx})|_\infty||\varphi||.\end{aligned}$$

Here, the bound depends on $|f^{(4)}|_\infty$. We note that $||\varphi_{xxx}||$ depends implicitly on $|f^{(4)}|_\infty$ through $||\varphi_{xt}||$, which is bounded by $||\varphi(\cdot,0)_{tt}||$ and hence by $||\varphi(\cdot,0)_{xxxx}||$. This procedure can be continued to obtain bounds of $||\varphi_{2mx}||$ and $||\varphi_{(2m-1)x}||$ that depend on derivatives in f up to $|f^{(2m)}|_\infty$.

Appendix B

In this appendix, we derive error estimates for the continuous error equation of (2.9) in 1D, assuming a finite domain with Dirichlet boundary condition. The continuous error equation for the *nth* order spatial discretization is given by

$$\begin{cases}ie_t=-v(ve)_{xx}+V_{PML}e+\Delta x^nT_e,\\e(x,0)=0.\end{cases}\tag{B.1}$$

Here n is assumed to be even and

$$T_e=\frac{c_n}{f}\frac{\partial^{n+2}}{\partial x^{n+2}}\left(\frac{1}{f}\varphi\right)=vc_n\frac{\partial^{n+2}}{\partial x^{n+2}}(v\varphi).\tag{B.2}$$

Then

$$\begin{aligned}\frac{\partial}{\partial t}||e||^2 &= (e,e_t)+(e_t,e)\\ &= \int i(ve^*)(ve)_{xx} - i(v^*e)(v^*e^*)_{xx} - i(V_{PML}-V_{PML}^*)e^*e - ie^*\Delta x^n T_e + i\Delta x^n T_e^* e.\end{aligned}$$

From (A.3) and (A.4), we get that

$$\begin{aligned}\frac{\partial}{\partial t}||e||^2 &= \int -4\alpha\beta e_x^* e_x + 2(\alpha\beta)_{xx}e^*e - 4\alpha_x\beta_x e^*e + 2\Im V_{PML}e^*e - ie^*\Delta x^n T_e + i\Delta x^n T_e^* e\\ &= \int -4\alpha\beta e_x^* e_x + (\alpha\beta)_{xx}e^*e - \alpha_x\beta_x e^*e - ie^*\Delta x^n T_e + i\Delta x^n T_e^* e. \qquad \text{(B.3)}\end{aligned}$$

In the layer, we have $\alpha \geq \alpha_0 > 0$. Then by (B.3)

$$\begin{aligned}\frac{\partial}{\partial t}||e||^2 &= \int -4\alpha\beta e_x^* e_x + (\alpha\beta)_{xx}e^*e - \alpha_x\beta_x e^*e - ie^*\Delta x^n T_e + i\Delta x^n T_e^* e\\ &= \int -4\alpha\beta e_x^* e_x + (\alpha\beta)_{xx}e^*e - \alpha_x\beta_x e^*e - ie^*\Delta x^n \Big(vc_n\frac{\partial^{n+2}}{\partial x^{n+2}}(v\varphi)\Big)\\ &\quad + i\Delta x^n \Big(vc_n\frac{\partial^{n+2}}{\partial x^{n+2}}(v\varphi)\Big)^* e.\end{aligned}$$

Integration by parts yields

$$\begin{aligned}\frac{\partial}{\partial t}||e||^2 &= \int -4\alpha\beta e_x^* e_x + (\alpha\beta)_{xx}e^*e - \alpha_x\beta_x e^*e + i\Delta x^n (e^* v c_n)_x \frac{\partial^{n+1}}{\partial x^{n+1}}(v\varphi)\\ &\quad - i\Delta x^n (v^* c_n^* e)_x \frac{\partial^{n+1}}{\partial x^{n+1}}(v\varphi)^*\\ &\leq \int -4\alpha\beta e_x^* e_x + (\alpha\beta)_{xx}e^*e - \alpha_x\beta_x e^*e + 2\Delta x^n\Big(\xi|e_x|^2 + \frac{1}{\xi}\Big|vc_n\frac{\partial^{n+1}}{\partial x^{n+1}}(v\varphi)\Big|^2\Big)\\ &\quad + 2\Delta x^n\Big(|e|^2 + \Big|v_x c_n\frac{\partial^{n+1}}{\partial x^{n+1}}(v\varphi)\Big|^2\Big)\\ &= (2\Delta x^n\xi - 4\alpha\beta)||e_x||^2 + \tilde{C}_2||e||^2 + 2\Delta x^n\Big(\frac{1}{\xi}\Big\|vc_n\frac{\partial^{n+1}}{\partial x^{n+1}}(v\varphi)\Big\|^2 + \Big\|v_x c_n\frac{\partial^{n+1}}{\partial x^{n+1}}(v\varphi)\Big\|^2\Big).\end{aligned}$$

We choose

$$\xi = \frac{\alpha_0\beta_0}{\Delta x^n},$$

so that

$$2\Delta x^n\xi - 4\alpha_0\beta_0 < 0.$$

Then the resulting ODE can be solved by integrating factor and we get the estimate

$$||e(\cdot,t)||^2 \leq \Delta x^n \tilde{K}(T), \qquad \text{(B.4)}$$

where

$$\tilde{K}(T) = e^{\tilde{C}_2 T}\int_0^T 2\Big(\frac{\Delta x^n}{\alpha_0\beta_0}\Big\|vc_n\frac{\partial^{n+1}}{\partial x^{n+1}}(v\varphi)\Big\|^2 + \Big\|v_x c_n\frac{\partial^{n+1}}{\partial x^{n+1}}(v\varphi)\Big\|^2\Big)e^{-\tilde{C}_2\tau}\mathrm{d}\tau,$$

so that $\tilde{K}(T)$ is bounded through the bounds on $||\varphi||_{H^{n+1}}$.

References

[1] T. Hagstrom, Radiation boundary condition for the numerical simulation of waves, Acta. Numerica., 8 (1999), 47–106.
[2] T. Hagstrom, New results on absorbing layers and radiation boundary conditions, Topics in computational wave propagation, Lecture Notes in Comput. Sci. Engrg., 31 (1999), 1–42.
[3] D. Givoli, Non-reflecting boundary conditions, J. Comput. Phys., 94 (1991), 1–29.
[4] I. Serban, J. Werschnik and E. K. U. Gross, Optimal control of time-dependent targets, Phys. Rev. A., 71 (2005), 053810.
[5] J. P. Berenger, A perfectly matched layer for the absorption of electromagnetic waves, J. Comput. Phys., 114 (1994), 185–200.
[6] X. Antoine, A. Arnold, C. Besse, M. Ehrhardt and A. Schädle, A review of transparent and artificial boundary conditions techniques for linear and nonlinear Schrödinger equations, Commun. Comput. Phys., 4 (2008), 729–796.
[7] S. Jiang and L. Greengard, Efficient representation of nonreflecting boundary conditions for the time-dependent Schrödinger equation in two dimensions, Comm. Pure. Appl. Math., 61 (2008), 261–288.
[8] B. Sjögreen and N. A. Petersson, Perfectly matched layers for Maxwell's equations in second order formulation, J. Comput. Phys., 209 (2005), 19–46.
[9] K. Kormann, S. Holmgren and H. O. Karlsson, Accurate time propagation for the Schrödinger equation with an explicitly time-dependent Hamiltonian, J. Chem. Phys., 128 (2008), 184101-1–184101-11.
[10] N. Moiseyev, Quantum theory of resonances: calculating energies, widths and cross-sections by complex scaling, Phys. Rep., 302 (1998), 211–293.
[11] H. O. Karlsson, Accurate resonances and effective absorption of flux using smooth exterior scaling, J. Chem. Phys., 109 (1998), 9366–9371.
[12] W. C. Chew and W. H. Weedon, A 3-D perfectly matched medium from modified Maxwell's equations with stretched coordinates, Micro. Opt. Tech. Lett., 7 (1994), 599–604.
[13] T. Sommerfeld and F. Tarantelli, Subspace iteration techniques for the calculation of resonances using complex symmetric Hamiltonians, J. Chem. Phys., 112 (1999), 2106–2110.
[14] H. O. Kreiss and J. Lorenz, Initial-Boundary Value Problems and the Navier-Stokes Equations, Society for Industrial and Applied Mathematics, Philadelphia, PA, 2004.
[15] K. Kormann and A. Nissen, Error control for simulations of a dissociative quantum system, Proceedings of ENUMATH 2009, the 8th European Conference on Numerical Mathematics and Advanced Applications, Uppsala, Sweden, June 29–July 3, 2009.
[16] J. C. Strikwerda, Finite Difference Schemes and Partial Differential Equations, Second Edition, Society for Industrial and Applied Mathematics, Philadelphia, PA, 2004.
[17] B. Gustafsson, H-O. Kreiss and J. Oliger, Time-Dependent Problems and Difference Methods, John Wiley & Sons, Inc., 1995.